Computers, Materials & Continua

Tech Science Press

https://doi.org/10.32604/cmc.2026.089644

ARTICLE

Cooperative Control of Fast Bus Transfer Using Cross-Modal Perception and an Event-Triggered Multi-Agent System

Pengyu Qian[1], Gangshuo Yuan[2], Pingpeng Tang[3], Xiangyu Zhang[3,4,*] and Lei Zhang[5]

[1]State Nuclear Electric Power Planning Design & Research Institute Co., Ltd., Beijing, China
[2]State Key Laboratory of Multimodal Artificial Intelligence Systems, Institute of Automation, Chinese Academy of Sciences, Beijing, China
[3]School of Ocean Engineering, Harbin Institute of Technology, Weihai, China
[4]Harbin Institute of Technology Qingdao Research Institute, Qingdao, China
[5]Wuhan Second Ship Design and Research Institute, Wuhan, China

*Corresponding Author: Xiangyu Zhang. Email: 24s130473@stu.hit.edu.cn

Received: 22 July 2026; Accepted: 04 October 2026; Published: 24 November 2026

ABSTRACT: Auxiliary bus transfer in an Advanced Passive 1000 (AP1000) nuclear power unit must satisfy the short permissible voltage-loss duration of the reactor-coolant-pump variable-frequency drive (VFD) despite non-monotonic bus residual voltage and nonlinear phase-angle drift. This paper evaluates a multimodal multi-agent framework for fast-transfer candidates and delayed backup-transfer cases. It fuses electrical waveforms, topology states, and protection logic to predict residual-voltage magnitude and phase angle. Candidate closing instants are screened using the wrapped phase-angle difference and resultant motor-bus voltage-to-frequency ratio (V/Hz), whereas the resulting motor and incoming-breaker inrush currents and protection responses are assessed offline in ETAP after each candidate event is applied. Six three-phase short-circuit conditions are evaluated using Electrical Transient Analyzer Program (ETAP)–Python co-simulation for a 1266 MW unit. Under the baseline event schedule, Condition 6 is the only condition in which the earliest permitted standby-source breaker (M2) event occurs below the 100 ms target, at 88.3 ms. Conditions 1–4 reach 103.3 ms, whereas Condition 5 is a breaker-failure backup case with an earliest permissible closing instant of 283.3 ms and an offline delayed candidate event at approximately 300 ms. Thus, full compliance with the 100 ms target has not been established under the current timing configuration. Compared with conventional fixed logic, the co-simulation reduces the average closing phase-angle difference from 21.92° to 12.62° and limits the maximum resultant motor-bus V/Hz to 1.29 p.u. under the adopted 1.33 p.u. criterion. The predictor achieves a mean phase-angle error of 2.4° at a 5 ms horizon. However, because the measured mean inference time is 8 ms, the results are interpreted as an offline prediction benchmark rather than evidence of a real-time end-to-end controller.

KEYWORDS: Fast bus transfer; AP1000; multi-agent systems; event-triggered communication; cross-modal fusion; residual-voltage prediction

1 Introduction

Reliable nuclear-unit operation depends on auxiliary-power-system stability. Following a short circuit on the working-source side, a trip, or voltage loss, fast bus transfer must disconnect the affected source and connect the standby source promptly while satisfying synchronism conditions. Nuclear-plant transfer therefore requires joint consideration of standby-source availability, bus residual voltage, phase-angle drift, and motor re-acceleration inrush current [1–3].

Copyright © 2027 The Authors. Published by Tech Science Press. This work is licensed under a Creative Commons Attribution 4.0 International License, which permits unrestricted use, distribution, and reproduction in any medium, provided the original work is properly cited.

The Advanced Passive 1000 (AP1000) nuclear-island reactor coolant pump is driven by a dedicated variable-frequency drive (VFD). Motor-group residual voltage and drive tolerance depend on machine inertia, load composition, voltage-dip duration, and direct-current (DC)-link parameters and protection settings [4,5]. Project data define approximately five cycles (about 100 ms) as the target following loss of power to the main-pump VFD. The Electrical Transient Analyzer Program (ETAP) event record provides fault-inception and breaker-state times; the analysis therefore distinguishes fast-transfer cases, cases near the timing boundary, and backup-transfer cases.

Bus transfer must account for the coupled dynamics of rotating machines and power-electronic equipment. Motor-group residual voltage depends on machine parameters, inertia, load composition, and isolation time [4], while the VFD rectifier, DC-link capacitance, load ratio, and protection settings introduce nonlinear voltage-dip behaviour [5]. In the ETAP model, this coupling produces a flat top, slow decay, local rise, and subsequent slow decay: a trajectory that cannot be captured by a pure-motor exponential model. The initial working-to-standby-source phase-angle differences of 33.42° under normal operation and 38.94° under the Haiyang 500 kV "channel N-1" condition are measured engineering inputs, not universal values.

Prior studies have examined bus-transfer modes, motor-transfer torque, breaker failure, residual-voltage constraints, and nuclear-plant transients [6–10]. Recent multi-agent research covers microgrid coordination and event-triggered control [11,12]. Graph-based methods address transient assessment under missing data and topology changes [13–15]; cross-modal attention supports fault-feature fusion [16]; and topology-aware graph convolutional network (GCN), long short-term memory (LSTM), and multimodal Transformer models provide suitable feature encoders [17–19]. Studies of substation communication and automatic bus transfer inform the messaging design [20–23]. Integrating these methods for nuclear-plant fast transfer under a short delay constraint motivates the present evaluation.

This paper evaluates a multi-agent coordination framework with multimodal perception for protection and switching coordination and offline closing-window assessment under nonlinear VFD residual voltage. Its contributions are as follows: (1) software abstractions of protection, breaker, and load-group functions, with event-triggered communication and separate analyses of communication and decision overheads; (2) a 5 ms one-step residual-voltage and phase-angle benchmark that fuses waveform, topology, and logic features, together with a deployment-oriented multi-horizon formulation; and (3) candidate closing-window assessment using phase angle, resultant motor-bus voltage-to-frequency ratio (V/Hz), and inrush current in six three-phase short-circuit simulations.

2 Physical Basis and Problem Formulation

2.1 AP1000 Auxiliary Power System Topology and Transfer Operating Characteristics

The system modelled in the co-simulation is a 1266 MW AP1000 unit in China. According to the site-specific primary-system data, the model contains six 10.5 kV medium-voltage bus sections (ES-1 through ES-6), and the working and standby sources are connected through auxiliary transformers on the 500 kV and 220 kV sides, respectively. These voltage levels, bus functions, and load lists are project-specific engineering data and are not presented as generic AP1000 design parameters. Published research shows that pressurised-water-reactor nuclear units exhibit coupled frequency, voltage, protection, and control responses during representative grid faults, requiring a validated integrated unit–grid model and a coordinated protection and control strategy [3]. The present study focuses on auxiliary bus transfer and the nonlinear VFD residual-voltage process.

The YNd11 transformer connection introduces an inherent phase shift on the 10 kV bus. During transfer, the working supply path through the main transformer (MT) and unit auxiliary transformer (UAT) is

replaced by the 220 kV standby path through the reserve auxiliary transformer (RAT). With line and leakage-reactance voltage drops included, the measured steady-state phase-angle difference is 33.42° under normal operating conditions. The SEL-351 relay performs synchronism discrimination and sequentially trips the working-source breaker M1 before closing the standby-source breaker M2; its relay output-signal hold time is at most 700 ms.

2.2 Four-Stage Division of the Fault Transfer Transient Process

The fault-transfer transient comprises four stages, as shown in Fig. 1.

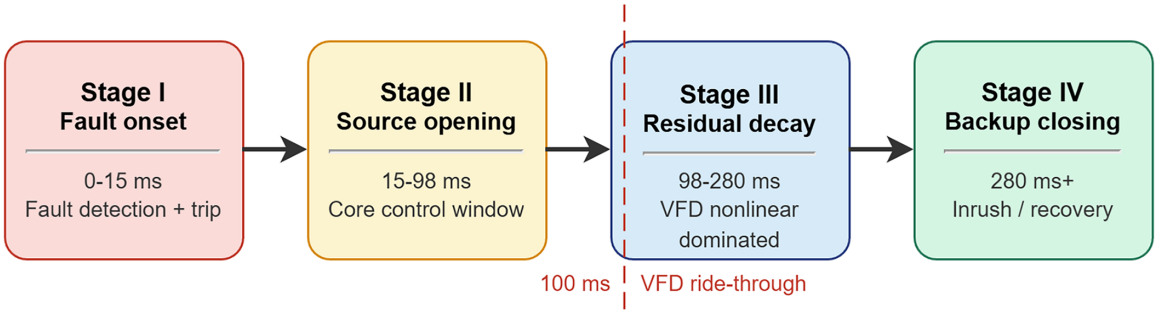

Figure 1: Four stages of the fault-transfer transient. VFD denotes variable-frequency drive.

Stage I is the fault-initiation stage. From fault inception on the working-source side to operation of the working-source breaker, the bus voltage drops rapidly, the motor loads begin to coast, and the VFD enters a low-voltage ride-through state. The principal control requirement is rapid fault discrimination and trip-signal generation. Stage II is the source-disconnection stage. From operation of the working-source breaker to closing of the standby-source breaker, the bus is disconnected from its external supply; residual-voltage magnitude, frequency, and phase angle together determine whether synchronous closing is permissible. Stage III is the residual-voltage decay stage, during which the rotating machines and VFD energy storage jointly maintain the bus residual voltage. This stage overlaps with Stage II in time.

Stage IV is the standby-source closing stage, in which the synchronism criterion is used to identify a candidate command and the co-simulation evaluates motor re-acceleration and VFD recovery. This paper uses 100 ms as the project target for conventional fast transfer and reports events beyond this boundary as cases near the timing boundary or as backup-transfer cases [2,6,7].

2.3 VFD Nonlinear Residual Voltage Mechanism

After source isolation, the rotating-machine group and VFD jointly determine the residual voltage. During a prolonged protection and arc-clearing interval, as in Condition 5, the same coupled subsystem can also produce a local rise before complete current interruption. Rectifier/DC-link coupling produces a model-dependent flat top, capacitor storage changes the decay rate, and coasting-motor/VFD energy exchange is consistent with the observed local rise [4,5]. The signal-driven predictor uses the resulting "flat top → slow decay → secondary rise → slow decay" trajectory as an observable feature. Configuration-level comparisons among pure-motor-group, single-VFD, and mixed-load configurations are reported in Supplementary Material S1; they are not treated as an exact internal-component decomposition.

2.4 Multimodal Data Definition of the Transfer Transient Process

Voltage-amplitude and frequency-difference criteria alone are insufficient for characterising nonlinear residual-voltage behaviour. This paper represents the transfer transient using three complementary modalities:

(1) The time-series waveform modality M_1 contains the instantaneous three-phase voltage and current waveforms of the 10 kV bus and the VFD DC-side voltage waveform. These signals are sampled at up to 10 kHz and represent the continuous electromagnetic transient process.

(2) The spatial topology modality M_2 represents node and branch relationships and graph mutations caused by the states of the generator circuit breaker (GCB), M1, and M2.

(3) The discrete-symbol modality M_3 encodes the discrete-event logic of trip commands, breaker-failure signals, and closing-permission signals issued by protective relays such as the GE G60, GE T60, and SEL-351.

The three modalities provide complementary information: M_3 identifies protection actions, M_1 tracks the residual-voltage trajectory, and M_2 represents electrical-distance changes. Their stage-dependent relevance motivates cross-modal fusion.

3 Proposed Multimodal Event-Triggered Multi-Agent Method

For a target time window of the order of 100 ms, centralised control may encounter communication bottlenecks, single-point failure, and stale state updates. This paper constructs a distributed multi-agent system (MAS) that maps the transfer-related equipment to three types of heterogeneous agent; the overall architecture is shown in Fig. 2. The architecture is evaluated as a means of reducing communication and decision overheads [11,12].

3.1 Agent Definition and Three-Layer Architecture

The proposed architecture comprises a physical control layer, a multi-agent interaction layer, and a multimodal perception and cooperative-decision layer. The physical layer contains the dual-source system, transformers, buses, breakers, main-pump VFD, and motor group. The interaction layer defines three heterogeneous agents:

(1) Perception-and-decision agent A_{PD}: a software abstraction of the SEL-351 protection and control functions that performs preprocessing, prediction, safety-domain evaluation, and candidate closing-decision generation in the co-simulation.

(2) Execution agent A_{EX}: a breaker abstraction that returns breaker-contact states and action-delay estimates to A_{PD}.

(3) Environment agent A_{EN}: an abstraction of the VFD and motor groups and their measurement interface that supplies synchronised continuous-measurement features to A_{PD}.

The implemented communication network contains nine agent instances: one A_{PD}; three A_{EX} instances associated with GCB, M1, and M2; and five A_{EN} instances associated with ES-1, ES-2, ES-3, the combined ES-4/ES-5 measurement group, and ES-6. These communication endpoints are distinct from the electrical graph nodes and adjacency matrix used by the GCN in Section 3.4. The upper multimodal perception and cooperative-decision layer fuses the three modalities, predicts residual voltage and phase angle, and applies the multi-objective criterion to generate a candidate closing decision. The layers exchange updates through the event-triggered mechanism [12].

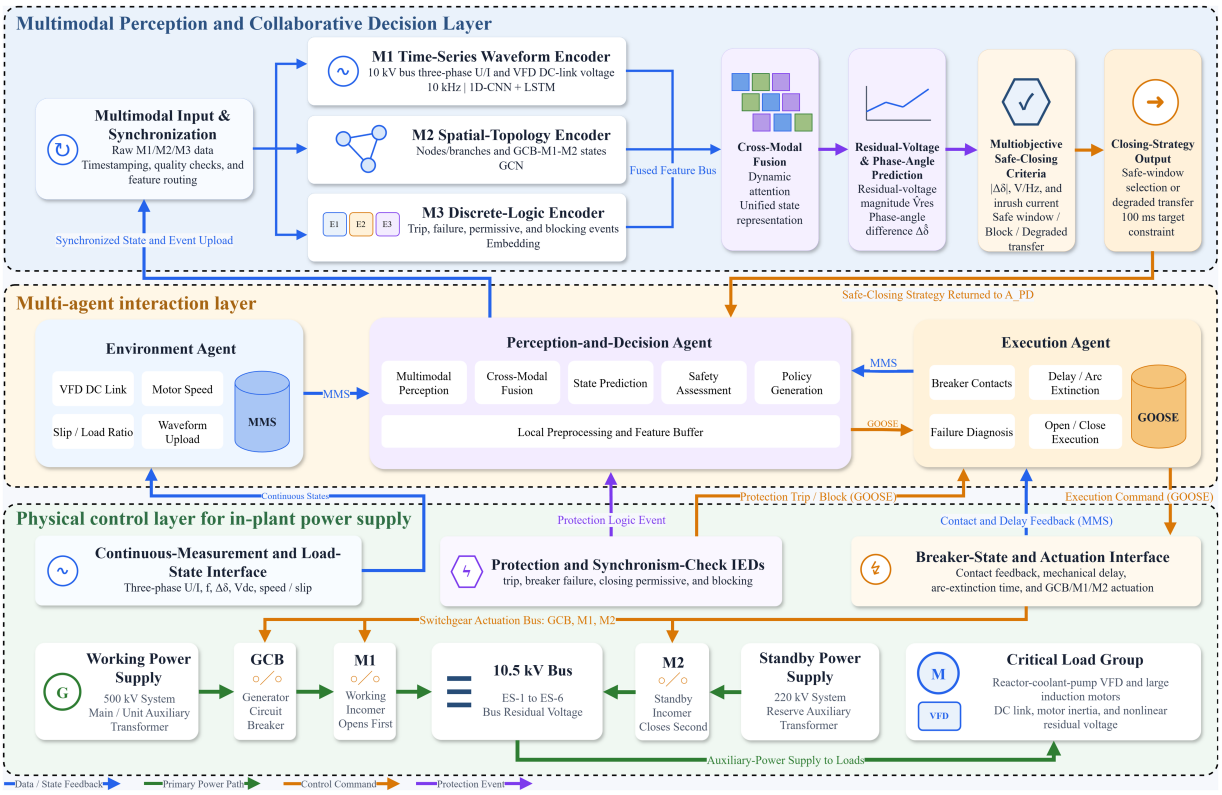

Figure 2: Three-layer multi-agent coordination architecture evaluated in offline co-simulation for auxiliary bus transfer. VFD, GCN, LSTM, GOOSE, and MMS denote variable-frequency drive, graph convolutional network, long short-term memory, generic object oriented substation event, and manufacturing message specification, respectively.

3.2 Agent Interaction and Communication Data Flow

The implemented paths are summarised in Table 1.

The interaction rules separate measurement, equipment execution, and candidate closing decisions. Through the continuous-measurement interface, the environment agents A_{EN} send synchronised voltage/current windows, frequency, the system-level phase-angle difference $\Delta\delta$, VFD status, and motor-group state to A_{PD}. Here, $\Delta\delta$ is derived from the synchronised voltage phasors of the monitored bus and standby source; it is not calculated or reported by a breaker agent. The execution agents A_{EX} report only breaker position, trip completion, and action-delay estimates. After aligning these inputs with protection events, A_{PD} updates the topology graph, predicts the residual-voltage trajectory, screens candidate instants using the predicted phase-angle difference and resultant V/Hz, and sends a time-stamped candidate-event record to A_{EX} for co-simulation. GOOSE carries time-critical commands and candidate events, whereas MMS carries measurement features and equipment-status feedback; a topology mutation triggers a new aligned snapshot before fusion. After the candidate event is applied, ETAP calculates the motor and incoming-breaker inrush currents and checks compliance with protection settings. These quantities are offline post-evaluation results and are not predictor outputs or causal inputs available before closing in the present study.

Table 1: Information exchanged among the perception-and-decision agent (A_{PD}), execution agents (A_{EX}), and environment agents (A_{EN}). GOOSE and MMS denote generic object oriented substation event and manufacturing message specification, respectively.

Information Path	Principal Content	Update Condition	Message Type
$A_{\mathrm{EN}} \rightarrow A_{\mathrm{PD}}$	Synchronised voltage/current window, frequency, $\Delta\delta$, VFD and motor-group status	Threshold crossing or requested feature update	MMS feature/status record
$A_{\mathrm{EX}} \rightarrow A_{\mathrm{PD}}$	Breaker position, trip completion, action-delay estimate	Command receipt or contact-state change	MMS status-feedback record
$A_{\mathrm{PD}} \rightarrow A_{\mathrm{EX}}$	Time-stamped candidate event for co-simulation	Predicted phase-angle difference and resultant V/Hz criteria are satisfied	GOOSE-formatted candidate event record

3.3 Event-Triggered Communication and Cooperative Decision-Making

The event mechanism serves as the communication scheduler for cooperative decision-making. A_{EX} status updates are generated upon receipt of a command or a change in contact state and do not use the phase-angle trigger. The synchronised phase-angle input is a single system-level quantity rather than a set of independent neighbour estimates. Accordingly, A_{PD} evaluates the scalar trigger at the ETAP sampling instant t_k by comparing the current phase-angle difference with the value at its last accepted trigger instant:

$$e_{\mathrm{PD}}(t_k) = \left|\Delta\delta(t_k) - \Delta\delta(t_{\mathrm{PD}}^{\mathrm{last}})\right| - \sigma_{\mathrm{PD}} \tag{1}$$

where $\Delta\delta(t_k)$ is the synchronised phase-angle difference supplied through A_{EN}, $t_{\mathrm{PD}}^{\mathrm{last}}$ is the last accepted trigger instant, and $\sigma_{\mathrm{PD}} > 0$ is the threshold. When $e_{\mathrm{PD}}(t_k) > 0$, the aligned multimodal state is made available for the cooperative decision update. The selected threshold is $\sigma_{\mathrm{PD}} = 2.0°$; its communication–accuracy sensitivity is reported in Supplementary Material S2. Because the scheduler is evaluated on the 10 kHz ETAP sample grid and permits at most one accepted update per sample, its effective minimum inter-event time is $\tau_{\min} = T_s = 0.1\,\mathrm{ms}$, so $t_{\mathrm{PD}}^{k+1} - t_{\mathrm{PD}}^{k} \geq \tau_{\min}$. This sampling-grid property excludes arbitrarily fast transmissions in the implemented discrete scheduler. It is not a continuous-time non-Zeno theorem or a Lyapunov proof of closed-loop consensus stability. The neighbourhood set N_i and communication-adjacency weights a_{ij} used in the previous generic expression are therefore not parameters of the implemented scalar trigger; this agent communication topology is also conceptually distinct from the electrical adjacency matrix used by the GCN.

Before disconnection of the working source, the monitored-bus phase follows the working-source phase. The initial working-to-standby-source phase-angle difference is therefore defined as:

$$\Delta\delta_0 = \theta_{\mathrm{work}} - \theta_{\mathrm{standby}} \tag{2}$$

where θ_{work} and $\theta_{\mathrm{standby}}$ are the source phase angles. After source disconnection, $\Delta\delta(t)$ denotes the phase-angle difference between the residual bus voltage and the standby-source voltage. The virtual experiment evaluates four initial offsets: +33.42°, −33.42°, +38.94°, and −38.94°. The summarised records are provided in Supplementary Material S3.

3.4 Cross-Modal Feature Extraction

For the three data modalities acquired by A_{PD}, dedicated neural networks are used for dimensionality reduction and feature mapping. For the time-series waveform modality M_1, a one-dimensional convolutional neural network (1D-CNN) with rectified linear unit (ReLU) activation and an LSTM network extracts features from the post-fault sequence $U(t)$ [18]:

$$H_{\mathrm{wave}} = \mathrm{LSTM}(\mathrm{ReLU}(\mathrm{Conv1D}(U(t);\ W_c))) \tag{3}$$

where W_c is the convolution-kernel parameter. The Conv1D layer extracts local waveform features, and the LSTM layer captures temporal dependencies in residual-voltage decay.

For the spatial topology modality M_2, the auxiliary-power node admittance matrix under the current breaker state is converted into an undirected graph $G = (V, E)$. Drawing on topology-aware transient-assessment methods [13–15,17], a graph convolutional network (GCN) extracts spatial electrical-distance features:

$$H_{\mathrm{topo}} = \mathrm{ReLU}\left(\tilde{D}^{-\frac{1}{2}}\tilde{A}\tilde{D}^{-\frac{1}{2}}XW_g\right) \tag{4}$$

where A is the adjacency matrix, I is the identity matrix, $\tilde{A} = A + I$, $\tilde{D}$ is the degree matrix, X is the node-feature matrix, and W_g is trainable. The GCN aggregates neighbouring states to represent fault-propagation paths and breaker-induced topology changes.

For the discrete-symbol modality M_3, events issued by the protective relays—such as trip commands, closing-permission signals, and breaker-failure indications—are encoded as learnable embedding vectors H_{logic}, allowing the discrete logic to be aligned with continuous features in the same space.

3.5 Cross-Modal Prediction and Deployment Horizon

Because the importance of different modalities varies across transient stages, a cross-modal attention mechanism is introduced for adaptively weighted fusion. The design draws on recent cross-modal attention fusion for power-grid fault diagnosis [16] and multimodal Transformer modelling [19]; its computation uses scaled dot-product attention, as shown in Eq. (5):

$$\mathrm{Attention}(Q, K, V) = \mathrm{softmax}\left(\frac{QK^{\mathrm{T}}}{\sqrt{d_k}}\right)V \tag{5}$$

where Q, K, and V are the query, key, and value matrices, respectively, and d_k is the key-vector dimension. The waveform feature H_{wave} is the query, while the topology and logic features are projected into key and value representations. The fused vector F_{fusion} enters a multi-layer perceptron (MLP) that outputs residual-voltage magnitude $\hat{V}_{\mathrm{res}}$ and phase-angle difference $\hat{\Delta\delta}$ at a prediction horizon of Δt [19]:

$$[\ \hat{V}_{\mathrm{res}},\ \hat{\Delta\delta}\ ] = \mathrm{MLP}(F_{\mathrm{fusion}}) \tag{6}$$

The evaluated one-step horizon is $\Delta t = 5$ ms, distinct from the 0.1 ms sampling interval and 2 ms window stride. For deployment, the relevant endpoint is M2 contact closure. Let t_k denote the last valid input time. The prediction horizon required to cover the 99th-percentile end-to-end (E2E) delay is

$$H_{\mathrm{req}} \geq T_{\mathrm{E2E},99} + T_{\mathrm{margin}}, \tag{7}$$

where $T_{\mathrm{E2E},99}$ comprises feature alignment, communication, inference, decision logic, output-relay operation, and M2 mechanical motion, and T_{margin} is a timing margin. The deployment-oriented output is

$$\widehat{\mathcal{Y}}_k = \left\{\left[\hat{V}_{\mathrm{res}}(t_k + jT_p), \hat{\Delta\delta}(t_k + jT_p)\right]\right\}_{j=1}^{K}. \tag{8}$$

Here, $T_p = 5$ ms is the prediction-grid interval and $K = \lceil H_{\mathrm{req}}/T_p \rceil$. The present study defines this multi-horizon output as a deployment-oriented extension and evaluates the underlying 5 ms one-step predictor in the virtual experiment.

3.6 Multi-Objective Candidate Closing Criterion

The proposed method first screens candidate closing windows using the predicted phase-angle difference and resultant motor-bus V/Hz; candidate-specific inrush is then evaluated offline in ETAP after the candidate event is applied. The signed prediction is first mapped to $\hat{\Delta\delta}_{\mathrm{w}} = \mathrm{wrap}_{[-180°,180°)}(\hat{\Delta\delta}_{\mathrm{close}})$ and constrained by

$$\left|\hat{\Delta\delta}_{\mathrm{w}}\right| \le \theta_{\max} \tag{9}$$

where $\theta_{\max} = 30°$. Using the motor-bus reconnection criterion adopted from American National Standards Institute/National Electrical Manufacturers Association (ANSI/NEMA) C50.41-2012 (R2021) [24], the resultant V/Hz constraint is

$$E_R = \sqrt{E_S^2 + E_M^2 - 2E_S E_M \cos\left(\hat{\Delta\delta}_{\mathrm{w}}\right)} \le 1.33 \text{ p.u.} \tag{10}$$

where E_S is the standby-source V/Hz phasor magnitude in per unit, E_M is the motor-bus residual V/Hz phasor magnitude in per unit, and E_R is their resultant difference. Because V_s and V_r are per-unit voltage magnitudes in this paper, $E_S = V_s/(f_s/f_n)$ and $E_M = V_r/(f_r/f_n)$, where f_s is the standby-source frequency, f_r is the residual frequency estimated at the simulated candidate or diagnostic instant, and f_n is the rated frequency. The predictor does not contain an independent frequency output head. Instead, using two consecutive phase-angle predictions with interval T_p, we estimate

$$\hat{f}_r(t_k) = f_s + \frac{\mathrm{unwrap}\left[\hat{\Delta\delta}(t_k) - \hat{\Delta\delta}(t_k - T_p)\right]}{2\pi T_p}. \tag{11}$$

This finite-difference estimate is validated against the ETAP reference trajectory in Supplementary Material S3. It is a candidate-time co-simulation estimate, not an independently validated online frequency-prediction head. When the standby source is at rated frequency, $f_s = f_n$ and hence $E_S = V_s$. Recent motor-bus-transfer research also shows that phase difference, breaker operating speed, motor inertia, and bus V/Hz variation affect post-transfer transient torque [9].

The 1.33 p.u. threshold is applied as a motor-bus reconnection screen and is interpreted together with manufacturer-specific VFD voltage limits. Condition 5 reaches 1.29 p.u. under this definition.

The motor inrush current must also remain below the locked-rotor current, and the incoming-breaker inrush current must remain below the setting calculated as

$$I_{\mathrm{set}} = 1.2\left(I_{\mathrm{calc}} - I_{\mathrm{motor}} + I_{\mathrm{start}}\right) \tag{12}$$

where I_{calc} is the total calculated current, I_{motor} is the maximum calculated motor current, and I_{start} is the maximum motor starting current. This value is the short-time, short-delay protection setting. If the

inrush current briefly exceeds the setting but remains within the specified time range, the candidate is considered acceptable.

In the co-simulation, A_{PD} selects the candidate with the lowest resultant V/Hz and the phase-angle difference closest to zero. The neural predictor does not directly output the inrush current; the candidate-specific inrush is evaluated by ETAP after the candidate instant is selected. If no candidate satisfies all constraints, transfer is delayed and evaluated against the residual- or withstand-voltage criterion. The multi-horizon formulation maps this screening rule to a deployment-time contact window.

4 Simulation Setup and Evaluation Protocol

4.1 Co-Simulation Platform, Scenarios, and Timing Definitions

The virtual experiment couples an ETAP model of a 1266 MW AP1000 auxiliary-power system with the proposed algorithm through the ETAP user-defined model (UDM) and an external Python interface. The model includes double-cage-rotor motors, a rectifier–capacitor–inverter VFD representation, and 500/220 kV slack sources. ETAP exports 600-ms electromagnetic-transient records sampled at 10 kHz (6000 points) for each condition.

The medium-voltage motors use a double-cage model with stator resistance R_1, leakage reactance X_1, magnetising reactance X_m, inner-cage impedance R_2/X_2, outer-cage impedance R_3/X_3, slip s, and combined rotor and load inertia. The VFD representation retains the rectifier bridge, direct-current (DC) link capacitor, inverter bridge, load ratio, and undervoltage settings required to reproduce the non-monotonic residual-voltage response.

The six fault and timing cases are summarised in Table 2; the detailed reproducibility settings are listed in Table 3.

Table 2: Fault-clearing times and earliest permitted working-source breaker (M1) and standby-source breaker (M2) event times under six three-phase short-circuit conditions.

Condition	Fault Location	M1 Current Interruption and Fault-Clearing Time (ms)	Earliest M2 Closing Event (ms)
Condition 1	Auxiliary transformer ZAS-ET-2A branch X	98.3	103.3
Condition 2	Auxiliary transformer ZAS-ET-2A branch Y	98.3	103.3
Condition 3	Auxiliary transformer ZAS-ET-2B branch X	98.3	103.3
Condition 4	Auxiliary transformer ZAS-ET-2B branch Y	98.3	103.3
Condition 5	Main generator outlet bus (GCB failure)	278.3	283.3
Condition 6	Main step-up transformer high-voltage-side bus	83.3	88.3

Table 3: Reproducibility settings for the ETAP–Python virtual experiment and the 5 ms one-step prediction benchmark.

Protocol Item	Setting Used in the Reported Experiment
ETAP record	600 ms per condition, sampled at 10 kHz (6000 points)
Phase-angle scheduler	Scalar A_{PD} trigger; $\sigma_{\mathrm{PD}} = 2.0^{\circ}$; evaluated on the 0.1 ms sample grid with $\tau_{\min} = 0.1$ ms
Supervised windows	20 ms (200 points), 2 ms sliding step, 90% overlap; windows from one trajectory remain in one subset
Cross-validation	Six-condition LOSO-CV; five conditions for training and one for testing; 3:1 training/validation split
Model comparison	Comparable model-capacity budgets; ablations use five random seeds under the same split
Inference record	8 ms isolated mean on i7-12700H/RTX 3060; the number of repetitions, tail-latency values, and common-clock contact records were not retained

All times in Table 2 use fault inception as a common time origin. M1 current interruption denotes arc extinction and fault clearing; the final column adds the prescribed 5 ms electrical dead time. Under Condition 5, contact separation is completed at 265.4 ms, current interruption at 278.3 ms, and the dead time ends at 283.3 ms; a later candidate near 300 ms is evaluated as a backup-transfer candidate. Conditions 1–4 reach 103.3 ms, whereas Condition 6 reaches 88.3 ms. The two measured initial phase-angle offsets are evaluated in both leading and lagging configurations, giving ±33.42° and ±38.94°.

4.2 End-to-End Timing Boundary

The 100 ms engineering target and the 5 ms prediction grid represent distinct timing quantities and should therefore be evaluated separately.

For a transfer case c, the earliest electrically permissible candidate instant is

$$T_{\mathrm{base}}^{(c)} = T_{\mathrm{clear}}^{(c)} + T_{\mathrm{dead}}, \tag{13}$$

where $T_{\mathrm{clear}}^{(c)}$ is measured from fault inception to current interruption and $T_{\mathrm{dead}} = 5$ ms. This definition produces the 103.3, 283.3, and 88.3 ms values in Table 2. The algorithmic path is described separately as

$$T_{\mathrm{alg}} = T_{\mathrm{align}} + T_{\mathrm{comm}} + T_{\mathrm{infer}} + T_{\mathrm{decision}}, \tag{14}$$

where the terms denote multimodal alignment, message delivery, neural inference, and safety-domain evaluation. Output-relay and breaker-motion times must additionally be included when the endpoint is the physical M2 contact closure. In an online implementation, acquisition, communication, and rolling inference can overlap with protection and breaker motion; therefore, T_{base} and the mean value of each subprocess must not be simply added as though all components were serial.

The isolated mean inference time, measured using an Intel i7-12700H central processing unit (CPU) and an RTX 3060 graphics processing unit (GPU), is 8 ms and therefore exceeds the evaluated 5 ms prediction horizon. Accordingly, this study treats the 5 ms result as a fixed-grid one-step accuracy benchmark. Eqs. (7) and (8) define the deployment-oriented horizon required to cover an end-to-end timing interval, but the

present study does not measure a common-clock 99th-percentile sample-to-contact interval or experimentally validate the multi-horizon output. Model acceleration, asynchronous acquisition and inference, and buffered trajectory output are therefore implementation options for future deployment rather than demonstrated real-time functions.

The complete reproducibility record is provided in Supplementary Material S4.

5 Results and Analysis

5.1 Prediction Accuracy and Ablation Study

Panel (a) of Fig. 3 shows the non-monotonic bus-voltage trajectory for Condition 5. The exponential baseline misses the fault-connected recovery feature near 210 ms, whereas the proposed multimodal predictor tracks the ETAP reference through the local rise and subsequent decay. The waveform-only long short-term memory (LSTM) benchmark and the remaining ablations are reported in Table 4, which quantifies the contribution of topology, protection logic, and cross-modal attention at the 5 ms prediction horizon.

Relative to waveform-only LSTM, adding topology reduces phase error from 9.2° to 5.8° (37.0%) and magnitude error from 0.068 to 0.041 p.u. (39.7%). The topology graph is most informative after a breaker-state mutation because it changes the electrical paths used to interpret the same local waveform. Adding protection logic to the waveform input reduces the phase error to 6.5° by distinguishing the fault-clearing and transfer stages, but it does not describe electrical distance as directly as the topology modality.

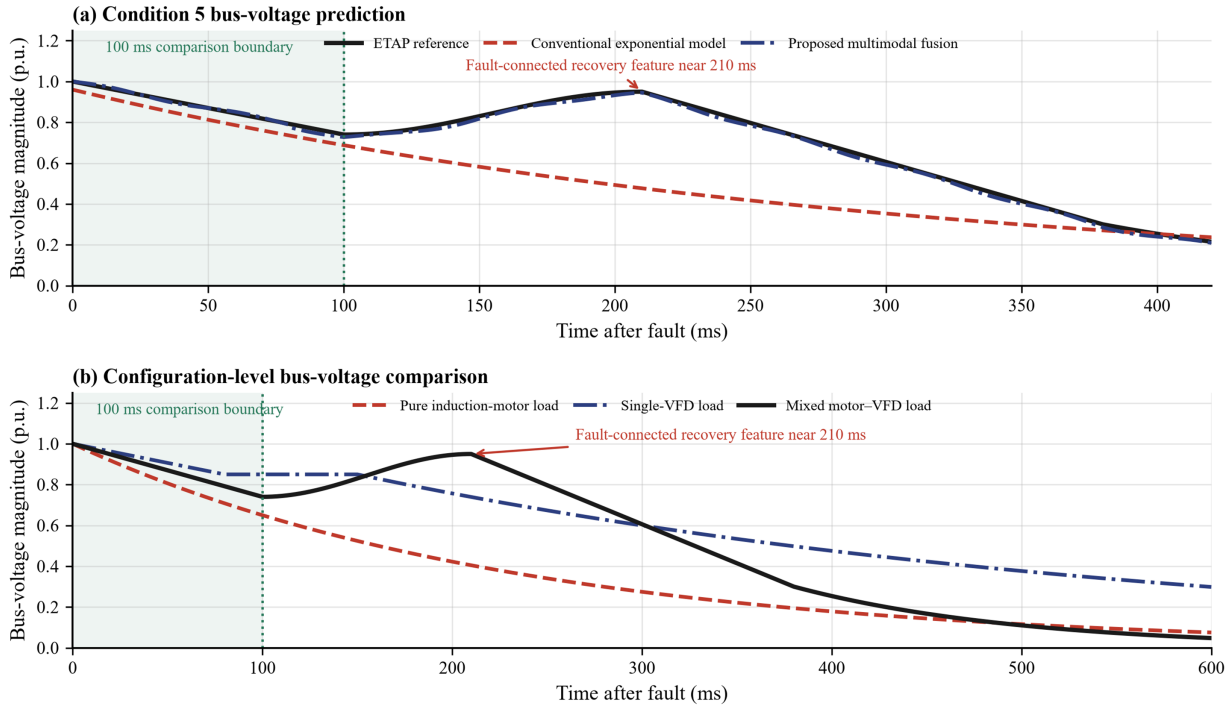

Figure 3: Bus-voltage prediction and configuration-level comparison under condition 5. Panel (**a**) Compares the electrical transient analyzer program (ETAP) reference, conventional exponential model, and proposed multimodal predictor; the numerical benchmark is evaluated at a one-step prediction horizon of 5 ms. Panel (**b**) Compares ETAP trajectories for pure-motor-group, single variable-frequency-drive (VFD), and mixed motor–VFD load configurations. The local rise near 210 ms is a fault-connected recovery feature rather than a post-isolation closing candidate; p.u. denotes per unit.

Table 4: Condition 5 prediction and ablation results together with the six-condition leave-one-scenario-out (LOSO) summary at the 5 ms one-step horizon. LSTM denotes long short-term memory; five-seed and LOSO entries are reported as mean ± standard deviation.

Configuration	Magnitude Error (p.u.)	Phase Error (°)	Evaluation
Exponential-decay baseline	0.142	18.5	Benchmark
Waveform-only LSTM	0.068	9.2	Benchmark
Waveform + topology	0.041 ± 0.005	5.8 ± 0.6	Five seeds
Waveform + logic	0.049 ± 0.006	6.5 ± 0.7	Five seeds
Three-modal, no attention	0.032 ± 0.004	3.9 ± 0.4	Five seeds
Full multimodal model	0.021 ± 0.004	2.4 ± 0.5	Five seeds
Six-condition LOSO mean	0.018 ± 0.002	1.91 ± 0.35	Six folds
Six-condition LOSO worst	–	3.65	Condition 5

The three-modal model without attention reaches 3.9 ± 0.4°, showing that joint feature availability already improves the predictor. Cross-modal attention further reduces the error to 2.4 ± 0.5° (38.5% relative to the no-attention model) and the magnitude error from 0.032 to 0.021 p.u. Rather than assigning a fixed modal weight throughout the transient, the attention mechanism is designed to adjust the relative contributions of waveform, topology, and logic features across transient stages. Prediction-level ablations are reported in Table 4; communication and decision performance is reported separately in Section 5.4. The lower block of Table 4 summarises the six held-out conditions: the mean magnitude and phase errors are 0.018 ± 0.002 p.u. and 1.91 ± 0.35°, respectively, and the worst reported phase error is 3.65° under Condition 5. The complete six-fold LOSO and seed records are provided in Supplementary Material S5, particularly Supplementary Table S5-A1.

5.2 Timing and Closing-Safety Results

Condition 5 is the severe backup case: conventional fixed logic produces a candidate instant near the simulated non-monotonic recovery region, whereas the proposed method selects a later candidate near 300 ms. The 283.3 ms value in Table 2 is the earliest electrically permissible event after fault clearing and dead time; the later candidate is used for the indicator comparison in Fig. 4 and Table 5. The feature near 210 ms occurs before contact separation at 265.4 ms and current interruption at 278.3 ms. It is therefore treated as a fault-connected recovery transient and diagnostic instant, not as a post-isolation closing candidate.

Across the six conditions, the proposed candidates reduce the mean phase-angle difference from 21.92° to 12.62° (42.4%). Under Condition 5, the phase-angle difference decreases from 45.6° to 24.3°, the resultant V/Hz decreases from 1.85 to 1.29 p.u., and the maximum inrush current decreases from 4250 to 1890 A. These results combine the pre-closing candidate-screening indicators (phase-angle difference and resultant V/Hz) with the corresponding offline ETAP post-evaluation of inrush current.

5.3 Residual-Voltage Characteristics and Physical Interpretation

The six cases show distinct decay patterns and secondary-peak timings, as summarised in Table 6. Condition 6 has the slowest decay and the earliest, smallest secondary peak, whereas Condition 5 has the longest clearing time and the largest delayed secondary peak.

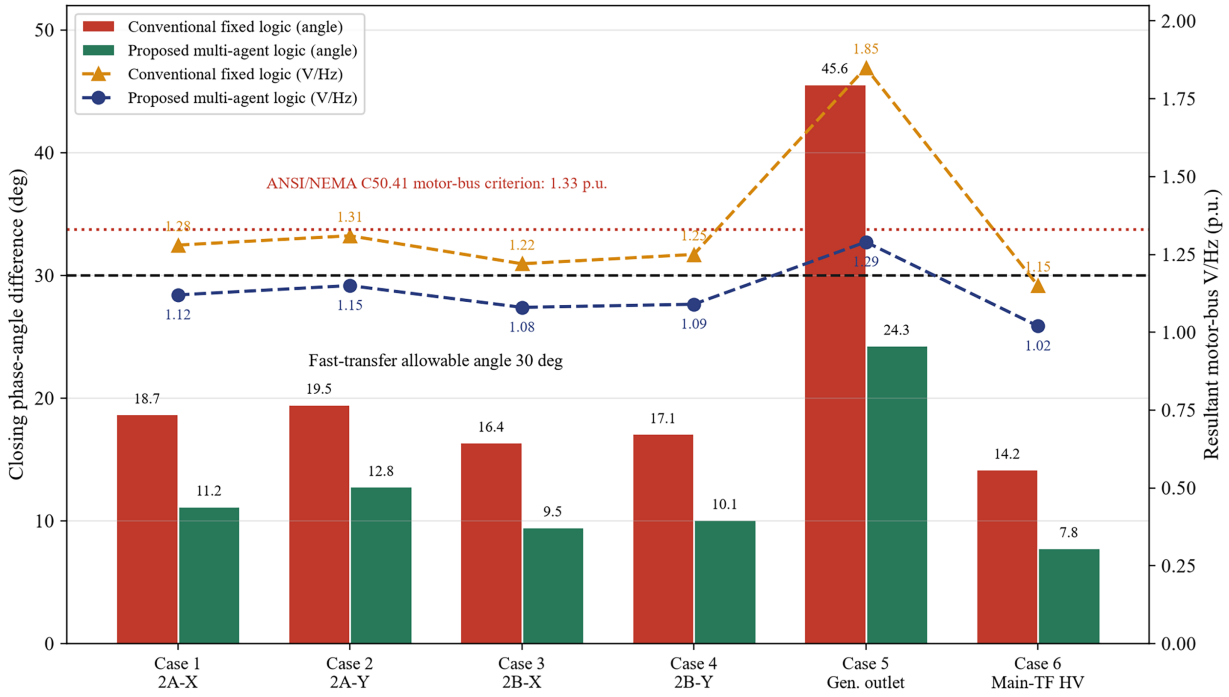

Figure 4: Combined comparison under six fault conditions. Bars and the left *y*-axis show the closing phase-angle difference; lines and the right *y*-axis show the resultant motor-bus V/Hz. The dashed lines mark the adopted 30° phase-angle and 1.33 p.u. V/Hz criteria. ANSI/NEMA denotes the American National Standards Institute/National Electrical Manufacturers Association. All values are from offline co-simulation candidates.

Table 5: Candidate-screening indicators and offline post-evaluation results under conventional (C) and proposed (P) strategies.

Condition	Phase-Angle Difference, C/P (°)	Resultant V/Hz, C/P (p.u.)	Maximum Inrush Current, C/P (A)
1	18.7/11.2	1.28/1.12	1450/1280
2	19.5/12.8	1.31/1.15	1510/1310
3	16.4/9.5	1.22/1.08	1350/1190
4	17.1/10.1	1.25/1.09	1380/1210
5	45.6/24.3	1.85/1.29	4250/1890
6	14.2/7.8	1.15/1.02	1200/1050

Table 6: Residual-voltage characteristics under the six simulated fault conditions.

Condition	Voltage at 100 ms (p.u.)	Secondary Peak (p.u.)	Secondary-Peak Time (ms)	Time to 0.3 p.u. (ms)
1	0.82	0.88	165	420
2	0.80	0.86	170	410
3	0.85	0.90	160	445
4	0.83	0.89	168	430
5	0.74	0.95	210	380
6	0.91	0.84	150	510

Panel (b) of Fig. 3 provides the configuration-level comparison under Condition 5. The pure-motor case reaches 0.65 p.u. at 100 ms and decays monotonically; the single-VFD case reaches 0.85 p.u. and exhibits a

flat-top feature; and the mixed-load case reaches 0.74 p.u. at 100 ms before the fault-connected secondary rise reaches 0.95 p.u. near 210 ms. The single-VFD flat top is consistent with rectifier/DC-link coupling, whereas the mixed-load local rise is consistent with coupled motor–VFD behaviour. These results connect the signal-driven predictor to the specified ETAP model without claiming an exact internal-component causal decomposition.

5.4 Communication and Network Assumptions

The network model uses IEC 61850 Generic Object Oriented Substation Event (GOOSE) messages for discrete commands and Manufacturing Message Specification (MMS) messages for feature and status exchange. Table 7 separates communication overhead from decision latency and reports mean, maximum, and 99th-percentile statistics under the same 100 Mbps configuration.

Table 7: Communication and decision statistics under fixed-period and event-triggered mechanisms.

Metric	Fixed-Period Polling	Event Triggering	Evaluation Scope
Protocol and link rate	GOOSE/MMS; 100 Mbps	GOOSE/MMS; 100 Mbps	Same configuration
Average message count	10	3	Per transfer cycle
Communication latency: mean/maximum/99th percentile (ms)	15.6/18.2/17.5	4.8/6.1/5.7	Communication only
Decision latency: mean/maximum/99th percentile (ms)	16.2/19.0/18.1	5.3/6.8/6.3	Excludes inference
Event-message length	64–128 bytes	64–128 bytes	Configured values
Feature-message length	512 bytes	512 bytes	Configured values

Compared with 10 ms polling, event triggering reduces the average message count from 10 to 3, communication overhead from 15.6 to 4.8 ms, and decision latency from 16.2 to 5.3 ms. Combining the mean isolated inference time of 8 ms with the other measured subprocesses yields an illustrative serial subtotal of 18.1 ms; this is not a common-clock end-to-end measurement. Under interface-level network injection, the reported phase error is 2.68 ± 0.61° with 5% random packet loss, 2.75 ± 0.65° under 0–5 ms jitter, and 3.15 ± 0.78° for the tested three-packet burst-loss case, with no violation of the evaluated safety criteria in the reported runs. These interface-level software injections are sensitivity tests only and do not substitute for hardware-in-the-loop experiments, real-time simulation, or validation on an actual IEC 61850 substation communication network.

The selected $\sigma_{PD} = 2.0°$ resulted in no missed triggers in the reported runs, whereas thresholds of 5.0° and above produced missed or delayed updates during Condition 5.

5.5 Initial Phase-Angle and Engineering Implications

The leading and lagging cases in Table 8 reproduce the two measured steady-state phase-offset magnitudes in leading and lagging configurations. The proposed candidates reduce all four closing-angle values; the −38.94° case remains slightly above the 30° criterion.

Table 8: Closing-angle comparison for leading and lagging initial phase states.

Initial State	Conventional Mean (°)	Proposed Candidate (°)	Status against the 30° Criterion
+33.42°, working source leading	16.26	9.70	Satisfied
−33.42°, working source lagging	65.28	29.15	Satisfied
+38.94°, N–1 leading	21.48	15.20	Satisfied
−38.94°, N–1 lagging	65.70	31.85	Exceeded

Aggregate network-uncertainty results are provided in Supplementary Material S6. For Conditions 1–4, the 98.3 ms fault-clearing interval plus 5 ms dead time produces 103.3 ms. Meeting 100 ms therefore requires earlier fault clearing or revised transfer logic; communication and computation optimisation acts on T_{alg}, not on the 3.3 ms excess in T_{base}.

6 Conclusions

This paper presents a multimodal prediction and event-triggered coordination method for AP1000 auxiliary bus transfer under nonlinear residual voltage. Waveform–topology–logic fusion reduces the Condition 5 phase error from 18.5° to $2.4 \pm 0.5°$ at the 5 ms benchmark. Event triggering reduces communication overhead from 15.6 to 4.8 ms and decision latency from 16.2 to 5.3 ms. Across the six simulated fault conditions, the proposed candidates reduce the mean closing-angle difference from 21.92° to 12.62° under the 1.33 p.u. V/Hz screen. Because Conditions 1–4 reach 103.3 ms, full compliance with the 100 ms target has not been demonstrated under the current timing configuration. The present results remain limited to offline ETAP–Python co-simulation and a 5 ms one-step prediction benchmark; they do not demonstrate a common-clock end-to-end real-time closing controller or a field-ready system. Hardware-in-the-loop or real-time-simulation experiments, synchronised hardware and network measurements, and validation on an actual or emulated substation network remain necessary before practical deployment.

Acknowledgement: Not applicable.

Funding Statement: The authors received no specific funding for this study.

Author Contributions: The authors confirm contribution to the paper as follows: Conceptualization, Pengyu Qian and Xiangyu Zhang; methodology, Pengyu Qian; validation, Pengyu Qian, Gangshuo Yuan and Pingpeng Tang; formal analysis, Pengyu Qian; investigation, Pengyu Qian and Gangshuo Yuan; resources, Pingpeng Tang and Lei Zhang; data curation, Pengyu Qian and Pingpeng Tang; writing—original draft preparation, Pengyu Qian; writing—review and editing, Xiangyu Zhang, Gangshuo Yuan, Pingpeng Tang and Lei Zhang; visualization, Pengyu Qian; supervision, Xiangyu Zhang; project administration, Xiangyu Zhang. All authors reviewed and approved the final version of the manuscript.

Availability of Data and Materials: The data supporting the findings of this study are available from the corresponding author upon reasonable request.

Ethics Approval: Not applicable.

Conflicts of Interest: The authors declare no conflicts of interest.

Supplementary Materials: The supplementary material is available online at https://www.techscience.com/doi/10.32604/cmc.2026.089644/s1.

References

1. Mazumdar S, Chiramal M. Bus transfer practices at nuclear plants. IEEE Trans Power Deliv. 1991;6(4):1438–43. doi:10.1109/61.97674.
2. Chang CK. A new MV bus transfer scheme for nuclear power plants. EPJ Nucl Sci Technol. 2015;1:9. doi:10.1051/epjn/e2015-50003-1.
3. Wang H, Li M, Sun P, Wei X. Research on protection control strategy of pressurized water reactor nuclear power units for typical power system faults. Ann Nucl Energy. 2024;201:110414. doi:10.1016/j.anucene.2024.110414.
4. Srivastava SC, Srivastava KN, Murty GN. Transient residual voltage analysis during isolated operation of a group of induction motor loads. Electr Mach Power Syst. 1994;22(2):289–309. doi:10.1080/07313569408955568.
5. Stockman K, D'hulster F, Verhaege K, Didden M, Belmans R. Ride-through of adjustable speed drives during voltage dips. Electr Power Syst Res. 2003;66(1):49–58. doi:10.1016/S0378-7796(03)00071-3.
6. Raje A, Raje A, McCall J, Chaudhary A. Bus transfer systems: requirements, implementation, and experiences. IEEE Trans Ind Appl. 2003;39(1):34–44. doi:10.1109/TIA.2002.807235.
7. Balamourougan V, Sidhu TS, Kasztenny B, Thakur MM. Robust technique for fast and safe transfer of power plant auxiliaries. IEEE Trans Energy Convers. 2006;21(2):541–51. doi:10.1109/TEC.2006.874231.
8. Chang CK. Adaptive undervoltage protection scheme for safety bus in nuclear power plants. Nucl Eng Technol. 2022;54(6):2055–61. doi:10.1016/j.net.2022.01.003.
9. Kim HS, Kim CH. Reduction method of transient torques on motors during motor bus transfer. J Electr Eng Technol. 2024;19(7):4045–57. doi:10.1007/s42835-024-01892-x.
10. Gusman LS, de Oliveira Neto JA. Analysis of the fast bus transfer applied to the APR1400 nuclear power plant. In: Proceedings of the XXV Congresso Brasileiro de Automática (CBA 2024); 2024 Oct 15–18; Rio de Janeiro, Brazil. Rio de Janeiro, Brazil: Sociedade Brasileira de Automática; 2024. doi:10.29327/1863744.1-69.
11. Izmirlioglu Y, Pham L, Son TC, Pontelli E. A survey of multi-agent systems for smartgrids. Energies. 2024;17(15):3620. doi:10.3390/en17153620.
12. Qu FR, Liu ZW, Liu X, Wang YW, Tian E. Memory-based event-triggered control for distributed secondary control in DC microgrids with quantized communication. IEEE Trans Ind Electron. 2024;71(11):14864–74. doi:10.1109/TIE.2024.3376793.
13. Zhao C, Jiao Z, Zhang P, Zhang L. Power system transient stability assessment based on hierarchical graph pooling method considering missing data. Int J Electr Power Energy Syst. 2025;172:111194. doi:10.1016/j.ijepes.2025.111194.
14. Ju Y, Li Z. Independent microgrid transient stability evaluation model based on a message passing graph neural network. IET Renew Power Gener. 2025;19(1):e70082. doi:10.1049/rpg2.70082.
15. Chen Q, Bu S, Wang H, Lei C. Real-time multi-stability risk assessment and visualization of power systems: a graph neural network-based method. IEEE Trans Power Syst. 2025;40(4):2955–68. doi:10.1109/TPWRS.2024.3524406.
16. Liu J, Duan Z, Liu H. A grid fault diagnosis framework based on adaptive integrated decomposition and cross-modal attention fusion. Neural Netw. 2024;178:106400. doi:10.1016/j.neunet.2024.106400.
17. Azad S, Ameli MT, Anvari-Moghaddam A, Shafie-khah M. A transfer learning-based graph convolutional network for dynamic security assessment considering loss of synchronism of wind turbines and unknown faults. e-Prime Adv Electr Eng Electron Energy. 2025;12:101012. doi:10.1016/j.prime.2025.101012.
18. Hochreiter S, Schmidhuber J. Long short-term memory. Neural Comput. 1997;9(8):1735–80. doi:10.1162/neco.1997.9.8.1735.
19. Tsai YHH, Bai S, Liang PP, Kolter JZ, Morency LP, Salakhutdinov R. Multimodal transformer for unaligned multimodal language sequences. In: Korhonen A, Traum D, Márquez L, editors. Proceedings of the 57th Annual Meeting of the Association for Computational Linguistics; 2019 Jul 28–Aug 2; Florence, Italy. Stroudsburg, PA, USA: Association for Computational Linguistics; 2019. p. 6558–69. doi:10.18653/v1/P19-1656.
20. Shi Z, Druzhinin Z. Development of 3-phase fault detection, protection, and automation application with the present of DG in AC power system using GOOSE protocol. Heliyon. 2024;10(6):e27482. doi:10.1016/j.heliyon.2024.e27482.

21. da Cruz AK, Kellermann ACH, da Silva IC, de Oliveira JMF, da Cruz MEJK, Däubler L. IEC 61850 GOOSE: a systematic literature review on the state of the art and current applications. Automation. 2026;7(2):62. doi:10.3390/automation7020062.
22. Nair NKC, Jenkins DLP. IEC 61850 enabled automatic bus transfer scheme for primary distribution substations. IEEE Trans Smart Grid. 2013;4(4):1821–8. doi:10.1109/TSG.2013.2285557.
23. Sevov L, Zhao T, Voloh I. The power of IEC 61850: bus-transfer and load-shedding applications. IEEE Ind Appl Mag. 2013;19(1):60–7. doi:10.1109/MIAS.2012.2215641.
24. National Electrical Manufacturers Association. Polyphase induction motors for power generating stations. ANSI/NEMA C50.41-2012 (R2021). Rosslyn, VA, USA: National Electrical Manufacturers Association; 2021.